

University of Nebraska - Lincoln

DigitalCommons@University of Nebraska - Lincoln

Anthony F. Starace Publications

Research Papers in Physics and Astronomy

February 2008

Attosecond pulse carrier-envelope phase effects on ionized electron momentum and energy distributions: roles of frequency, intensity and an additional IR pulse

Liang-You Peng

University of Nebraska - Lincoln & Peking University, Beijing

Evgeny A. Pronin

University of Nebraska - Lincoln, epronin2@unl.edu

Anthony F. Starace

University of Nebraska-Lincoln, astarace1@unl.edu

Follow this and additional works at: <https://digitalcommons.unl.edu/physicsstarace>



Part of the [Physics Commons](#)

Peng, Liang-You; Pronin, Evgeny A.; and Starace, Anthony F., "Attosecond pulse carrier-envelope phase effects on ionized electron momentum and energy distributions: roles of frequency, intensity and an additional IR pulse" (2008). *Anthony F. Starace Publications*. 112.

<https://digitalcommons.unl.edu/physicsstarace/112>

This Article is brought to you for free and open access by the Research Papers in Physics and Astronomy at DigitalCommons@University of Nebraska - Lincoln. It has been accepted for inclusion in Anthony F. Starace Publications by an authorized administrator of DigitalCommons@University of Nebraska - Lincoln.

Attosecond pulse carrier-envelope phase effects on ionized electron momentum and energy distributions: roles of frequency, intensity and an additional IR pulse

Liang-You Peng^{1,2}, Evgeny A Pronin¹ and Anthony F Starace¹

¹ Department of Physics and Astronomy, The University of Nebraska, Lincoln, NE 68588-0111, USA

² State Key Laboratory for Mesoscopic Physics and Department of Physics, Peking University, Beijing 100871, People's Republic of China

E-mail: astarace1@UNL.edu

New Journal of Physics **10** (2008) 025030 (21pp)

Received 20 October 2007

Published 29 February 2008

Online at <http://www.njp.org/>

doi:10.1088/1367-2630/10/2/025030

Abstract. The effects of the carrier-envelope phase (CEP) of a few-cycle attosecond pulse on ionized electron momentum and energy spectra are analyzed, both with and without an additional few-cycle IR pulse. In the absence of an IR pulse, the CEP-induced asymmetries in the ionized electron momentum distributions are shown to vary as the $3/2$ power of the attosecond pulse intensity. These asymmetries are also found to satisfy an approximate scaling law involving the frequency and intensity of the attosecond pulse. In the presence of even a very weak IR pulse (having an intensity of the order of 10^{11} – 10^{12} W cm⁻²), the attosecond pulse CEP-induced asymmetries in the ionized electron momentum distributions are found to be significantly augmented. In addition, for higher IR laser intensities, we observe for low electron energies peaks separated by the IR photon energy in one electron momentum direction along the laser polarization axis; in the opposite direction, we find structured peaks that are spaced by twice the IR photon energy. Possible physical mechanisms for such asymmetric, low-energy structures in the ionized electron momentum distribution are proposed. Our results are based on single-active-electron solutions of the three-dimensional, time-dependent Schrödinger equation including atomic potentials appropriate for the H and He atoms.

Contents

1. Introduction	2
2. Theoretical formulation	3
2.1. Solution of the TDSE	3
2.2. Projection onto momentum states	4
3. Roles of frequency and intensity on attosecond CEP effects	8
3.1. An approximate frequency–intensity scaling law	8
3.2. Intensity dependence of CEP-induced asymmetries	10
4. Role of an additional IR laser pulse	11
4.1. Augmentation of attosecond pulse CEP effects by a weak, few-cycle IR pulse	11
4.2. Low-energy structures appearing in the presence of an intense IR pulse	14
5. Summary and conclusions	20
Acknowledgments	20
References	21

1. Introduction

The experimental ability to produce attosecond pulses of such short duration that they comprise only a few cycles has recently been reported [1]. Moreover, the carrier-envelope phases (CEPs) of these attosecond pulses were reported to be stable and capable of being tuned, such as by using aluminium foils of variable thickness [1]. Interest in CEP-dependent effects of few cycle laser pulses has grown since the late 1990s (see, e.g. [2]–[4]). Since the first experimental demonstrations of CEP effects on photoelectron spatial distributions produced by 5 fs few-cycle laser pulses [5, 6], experimental and theoretical interest in CEP effects produced by sub-10 fs few-cycle laser pulses has increased enormously (see, e.g. [7]–[9] and references therein). In particular, analysis of asymmetric photoelectron distributions resulting from ionization by combined few-cycle infrared (IR) and attosecond extreme ultraviolet (XUV) pulses has been shown to allow the determination of the electric field of the few-cycle IR pulse [10, 11] or the duration of the XUV pulse [12]. Now that few-cycle attosecond pulses have become available with tunable CEPs, it is of interest to explore the kinds of CEP-induced effects on ionized electron momentum and energy distributions that are possible or, in other words, the kind(s) of control over the ionization process the CEP provides at these XUV photon energies. An initial investigation of ionized electron momentum and energy distributions produced by one or two (coherent) few-cycle attosecond pulses with independent, fixed CEPs has recently appeared [13]. It was found that such CEP-induced effects require attosecond pulses having intensities at or above the limit of current experimental capabilities (i.e. in the weak XUV pulse case, there are no such effects). In this paper, we extend these initial investigations by determining the scaling with frequency and intensity of the CEP-induced asymmetries in ionized electron momentum distributions. We also investigate here the role of an additional IR laser field on the energy and momentum distributions of electrons ionized by a few-cycle attosecond pulse with well-defined CEP. Note that ionized electron momentum distributions produced by an attosecond pulse train in the presence of an IR field have been recently measured experimentally and analyzed theoretically [14, 15]. Our focus here differs in studying ionization by a single attosecond pulse having only a few cycles, so that attosecond CEP effects are significant.

This paper is organized as follows: in section 2, we give a brief description of our theoretical method, which is based on the exact solution (within the single-active electron approximation) of the three-dimensional, time-dependent Schrödinger equation (TDSE) [13, 16]. This section includes a comparison of results obtained with projection of the numerical solution of the TDSE onto eigenstates of the field-free Hamiltonian (i.e. onto Coulomb waves) versus projection onto plane waves. In section 3, we present numerical evidence on the scaling with frequency and intensity of the asymmetries in ionized electron momentum and energy distributions induced by the CEP of the attosecond pulse. Results are presented for electrons ionized from both the H atom and the He atom. In section 4, we consider the effects of an additional few-cycle IR pulse on the asymmetries in the electron momentum and energy distributions resulting from ionization of the H atom by a few-cycle attosecond pulse with defined CEP. In section 5, we summarize our results and present some conclusions.

2. Theoretical formulation

In this section, we briefly describe our theoretical method, which is based on a direct solution of the TDSE. Additional details about the method can be found in [13, 16]. For the H atom, the atomic potential is simply the nuclear Coulomb potential. For the He atom, we employ the effective one-electron potential given by Hartree [17], which has been used by others to model the He atom in a strong laser field [18]. In this paper, all equations are given in atomic units ($\hbar = e = m_e = 4\pi\epsilon_0 = 1$) and the electromagnetic fields (and potentials) are assumed to be in SI units.

2.1. Solution of the TDSE

For a neutral atom having a single active electron that is ionized by an attosecond pulse in the presence of an additional IR pulse, the TDSE describing the active electron is

$$i\frac{\partial}{\partial t}\Psi(\mathbf{r}, t) = [H_0(\mathbf{r}) + H_1(\mathbf{r}, t)]\Psi(\mathbf{r}, t), \quad (1)$$

where H_0 is the field-free Hamiltonian, defined by

$$\begin{aligned} H_0 &= -\frac{1}{2}\nabla^2 + V_C(r) \\ &= -\frac{1}{2}\left[\frac{1}{r^2}\frac{\partial}{\partial r}\left(r^2\frac{\partial}{\partial r}\right) - \frac{1}{r^2}\hat{L}^2\right] + V_C(r), \end{aligned} \quad (2)$$

\hat{L}^2 is the square of the orbital angular momentum operator, and $V_C(r)$ is the effective atomic potential, which has a long-range Coulomb tail. For the cases of H and He, $V_C(r)$ is given explicitly by

$$V_C(r) = \begin{cases} -\frac{1}{r}, & \text{for H,} \\ -\frac{1}{r}[1 + (1 + \beta r/2)e^{-\beta r}], & \text{for He,} \end{cases} \quad (3)$$

where $\beta = 27/8$ [17].

The interaction of the active electron with the attosecond and IR laser pulses is described in equation (1) by $H_1(\mathbf{r}, t)$, whose expression may be given in either the length gauge or the velocity gauge. We adopt the velocity gauge in the present work, but we find that the results for the two gauges agree well. In the velocity gauge, $H_1(\mathbf{r}, t)$ is given by

$$H_1(\mathbf{r}, t) = -i\mathbf{A}_{\text{total}}(t) \cdot \nabla, \quad (4)$$

where $\mathbf{A}_{\text{total}}(t) = \mathbf{A}(t) + \mathbf{A}_{\text{IR}}(t)$ is the total vector potential for the attosecond and IR laser pulses. The attosecond pulse, with frequency ω and peak intensity I_0 , is assumed to be linearly polarized along the z -axis. Its vector potential is given by

$$\mathbf{A}(t) = A(t)\hat{\mathbf{z}} = A_0 F(t) \sin \left[\omega \left(t + \frac{\tau}{2} \right) + \phi \right] \hat{\mathbf{z}}, \quad (5)$$

where $A_0 = \sqrt{I_0/I_{\text{au}}}/\omega$, in which I_{au} is the atomic unit of intensity, i.e. $I_{\text{au}} = 3.509 \times 10^{16} \text{ W cm}^{-2}$ (which corresponds to the intensity of a monochromatic laser field having an electric field strength of one atomic unit). The CEP is ϕ and the pulse duration is $\tau = nT$ (where n is the integer number of cycles in the attosecond pulse and $T = 2\pi/\omega$ is the period). The XUV pulse vector potential envelope, $F(t)$, is given by

$$F(t) = \begin{cases} \sin^2[\pi(t + \tau/2)/\tau], & |t| \leq \tau/2; \\ 0, & |t| > \tau/2. \end{cases} \quad (6)$$

The IR pulse, with frequency ω_{IR} and peak intensity I_{IR} , is also assumed to be linearly polarized along the z -axis. Its vector potential is given by

$$\mathbf{A}_{\text{IR}}(t) = A_{\text{IR}}(t)\hat{\mathbf{z}} = A_{\text{IR}}^0 F_{\text{IR}}(t) \sin \left[\omega_{\text{IR}} \left(t + \frac{\tau_{\text{IR}}}{2} \right) + \phi_{\text{IR}} \right] \hat{\mathbf{z}}, \quad (7)$$

where $A_{\text{IR}}^0 = \sqrt{I_{\text{IR}}/I_{\text{au}}}/\omega_{\text{IR}}$. The IR pulse duration is $\tau_{\text{IR}} = n_{\text{IR}}T_{\text{IR}}$ (where n_{IR} is the integer number of cycles in the IR pulse and $T = 2\pi/\omega_{\text{IR}}$ is the period). The IR pulse phase, ϕ_{IR} , can be used to control whether one puts the attosecond pulse at the zero ($\phi_{\text{IR}} = 0$) or at the peak ($\phi_{\text{IR}} = 0.5\pi$) of the IR vector potential at $t = 0$. The IR vector potential envelope, $F_{\text{IR}}(t)$, is given by

$$F_{\text{IR}}(t) = \begin{cases} \sin^2[\pi(t + \tau_{\text{IR}}/2)/\tau_{\text{IR}}], & |t| \leq \tau_{\text{IR}}/2; \\ 0, & |t| > \tau_{\text{IR}}/2. \end{cases} \quad (8)$$

The TDSE (1) has been solved numerically in spherical coordinates using the Arnoldi method to propagate the wavefunction [13, 16]. The ground state wavefunction can be calculated by solving the TDSE in imaginary time as a diffusion equation (without any external fields) for an arbitrary initial trial wavefunction (see, e.g. [19]). In all the calculations whose results are presented below, we use the following spatial and temporal parameters: all angular momenta in the range $0 \leq l \leq 15$ are included; the radial grid spacing is $\Delta r = 0.1 \text{ au}$; the total number of radial grid points is $N_r = 24\,000$; the time step for propagation is $\Delta t = 0.01 \text{ au}$; and the Arnoldi propagator is of order $M = 30$.

2.2. Projection onto momentum states

In order to calculate the distribution of ionized electron (asymptotic) momenta and energies in the final state, we project the numerically calculated wavefunction onto the energy eigenstates of the field-free Hamiltonian, H_0 , i.e. onto incoming Coulomb waves, $\Psi_{\mathbf{k}}^{(-)}(\mathbf{r}, t_p)$, at a time t_p , which is some time after the interaction of the atom with the laser field(s) is over. The Coulomb wavefunction satisfying incoming wave boundary conditions may be written in general as

$$\Psi_{\mathbf{k}}^{(-)}(\mathbf{r}, t) = \frac{1}{\sqrt{k}} \sum_{lm} i^l e^{-i[\sigma_l(k) + \delta_l(k)]} Y_{lm}(\hat{\mathbf{r}}) Y_{lm}^*(\hat{\mathbf{k}}) R_{El}(r) e^{-iEt}, \quad (9)$$

where $\sigma_l(k) = \arg\Gamma(l + 1 + i\eta)$ is the Coulomb phase shift, $\eta = -(Z - N)/k$, Z is the nuclear charge, N is the number of electrons remaining in the ion, and $\delta_l(k)$ is the l th partial wave

phase shift (with respect to Coulomb waves) due to any non-Coulomb, short-range part of the potential. For the case of the H atom, the radial wavefunction is known analytically, so that

$$\Psi_{\mathbf{k}}^{(-)}(\mathbf{r}, t) = \sqrt{\frac{2}{\pi}} \sum_{lm} i^l e^{-i\sigma_l(k)} Y_{lm}(\hat{r}) Y_{lm}^*(\hat{k}) e^{-iEt} \\ \times \frac{2^l e^{-(\pi\eta/2)} |\Gamma(l+1+i\eta)|}{(2l+1)!} (kr)^l e^{-ikr} {}_1F_1(-i\eta+l+1, 2l+2, 2ikr), \quad (10)$$

where $\eta = -1/k$. The momentum space wavefunction is thus

$$\Upsilon(\mathbf{k}) = \langle \Psi_{\mathbf{k}}^{(-)}(\mathbf{r}, t_p) | \Psi(\mathbf{r}, t_p) \rangle. \quad (11)$$

Note that the size of the radial box within which one calculates the numerical solution of the TDSE must be large enough so that the highest momentum components of the numerically calculated electron wave packet do not reach the box edge (and get reflected) before the interaction of the atom with the laser fields is over.

Owing to the symmetry of k_x and k_y , one may set $k_y = 0$ without loss of generality. The transition probability to the final state $(k_x, k_y = 0, k_z)$ is calculated according to

$$P(k_x, k_z) = |\Upsilon(k_x, k_y = 0, k_z)|^2 = P(E, \theta_k), \quad (12)$$

where $E = (k_x^2 + k_z^2)/2$, and θ_k is the angle between the (asymptotic) electron momentum $\mathbf{k} = (k_x, 0, k_z)$ and the laser polarization axis, $\hat{\mathbf{z}}$. The total ionization probability is given by

$$P_t = \int_0^\infty dE \int_0^{2\pi} d\theta_k P(E, \theta_k) \\ = \int_{-\infty}^\infty dk_x \int_{-\infty}^0 dk_z P(k_x, k_z) + \int_{-\infty}^\infty dk_x \int_0^\infty dk_z P(k_x, k_z) \\ \equiv P_- + P_+, \quad (13)$$

where P_- (P_+) is the probability for electron ionization in the negative (positive) direction of \mathbf{k}_z . One may also define a normalized asymmetry factor [12],

$$R \equiv P_d/P_t = (P_- - P_+)/P_t, \quad (14)$$

where P_d is the difference (or asymmetry) between P_- and P_+ . (Alternatively, one may define an angle-dependent, normalized asymmetry parameter as the ratio of the difference and the sum of electrons ejected with angles θ and $\pi - \theta$ with respect to the z -axis (as, e.g. in [20]), which may prove simpler to measure experimentally.)

Note that $\Upsilon(\mathbf{k})$ and $P(E, \theta_k)$ do not depend on the moment of projection, t_p , because the incoming Coulomb waves, $\Psi_{\mathbf{k}}^{(-)}$, are energy eigenstates of the field-free Hamiltonian (2), i.e. one can write

$$\Psi(\mathbf{r}, t) = \int d\mathbf{k} \Upsilon(\mathbf{k}) \Psi_{\mathbf{k}}^{(-)}(\mathbf{r}, t) = \int d\mathbf{k} \Upsilon(\mathbf{k}) \Psi_{\mathbf{k}}^{(-)}(\mathbf{r}) e^{-iEt}, \quad (15)$$

for any t following the end of the interaction of the atom with the laser pulse(s). This contrasts with the Fourier transform of $\Psi(\mathbf{r}, t_p)$, i.e. with the projection of the numerically calculated

solution of the TDSE onto plane waves, which are energy eigenstates of only the kinetic energy part, $-\frac{1}{2}\nabla^2$, of the field-free Hamiltonian (2). In this latter case

$$\Psi(\mathbf{r}, t_p) = \int d\mathbf{k} \Upsilon^{\text{PW}}(\mathbf{k}, t_p) \Psi_{\mathbf{k}}^{\text{PW}}(\mathbf{r}, t_p) = \int d\mathbf{k} \Upsilon^{\text{PW}}(\mathbf{k}, t_p) \Psi_{\mathbf{k}}^{\text{PW}}(\mathbf{r}) e^{-iEt_p}, \quad (16)$$

where

$$\Upsilon^{\text{PW}}(\mathbf{k}, t_p) = \langle \Psi_{\mathbf{k}}^{\text{PW}}(\mathbf{r}, t_p) | \Psi(\mathbf{r}, t_p) \rangle. \quad (17)$$

The expansion of the plane-wave wavefunction in spherical harmonics is given by,

$$\begin{aligned} \Psi_{\mathbf{k}}^{\text{PW}}(\mathbf{r}, t) &= \frac{1}{(2\pi)^{3/2}} e^{i\mathbf{k}\mathbf{r}} e^{-iEt} = \sqrt{\frac{2}{\pi}} \sum_{l=0}^{\infty} \sum_{m=-l}^l i^l Y_{lm}(\hat{r}) Y_{lm}^*(\hat{k}) e^{-iEt} \\ &\times \frac{1}{(2l+1)!!} (kr)^l e^{-ikr} {}_1F_1(l+1, 2l+2; 2ikr), \end{aligned} \quad (18)$$

which is the usual expansion of a plane wave in terms of spherical Bessel functions, but with the latter expressed here in terms of the ${}_1F_1$ confluent hypergeometric functions. Thus, the Fourier transform of $\Psi(\mathbf{r}, t_p)$, i.e. the momentum space wavefunction $\Upsilon^{\text{PW}}(\mathbf{k}, t_p)$, depends on the moment t_p at which the projection is carried out. Substituting equation (15) (evaluated at $t = t_p$) into equation (17), one can extract this time dependence explicitly:

$$\Upsilon^{\text{PW}}(\mathbf{k}', t_p) = \int d\mathbf{k} \Upsilon(\mathbf{k}) \langle \Psi_{\mathbf{k}'}^{\text{PW}} | \Psi_{\mathbf{k}}^{(-)} \rangle e^{-i(E-E')t_p}. \quad (19)$$

In figure 1, we compare the two momentum space probability distributions, $|\Upsilon(\mathbf{k})|^2$ and $|\Upsilon^{\text{PW}}(\mathbf{k}, t_p)|^2$, where the corresponding momentum space wavefunctions are defined in equations (11) and (17). One observes that, on average, the two probability distributions agree well with each other, especially for larger ionized electron energies and longer times, t_p , following the end of the attosecond pulse. The rapid oscillations with increasing energy observed in the projections onto plane waves depend on the time, t_p , at which the projection is calculated. These rapid oscillations originate from the exponential time factor in equation (19). Thus, from equation (19) it is clear that the period of these oscillations should decrease in proportion to t_p^{-1} . In order to explain the fact that the amplitude of the oscillations is larger at lower energies, one must consider the properties of the term $\langle \Psi_{\mathbf{k}'}^{\text{PW}} | \Psi_{\mathbf{k}}^{(-)} \rangle$, i.e. the projection of the Coulomb wavefunction onto the plane wave wavefunction. For larger energies (or larger ionized electron momenta), $\lim_{k \rightarrow \infty} \langle \Psi_{\mathbf{k}'}^{\text{PW}} | \Psi_{\mathbf{k}}^{(-)} \rangle \rightarrow \delta(\mathbf{k} - \mathbf{k}')$, i.e. there is little difference between a plane wave and a Coulomb wave at high energies (compare equations (10) and (18), for $k \rightarrow \infty$ and $\eta \rightarrow 0$). Therefore, $\lim_{k \rightarrow \infty} |\Upsilon^{\text{PW}}(\mathbf{k}, t_p)|^2 \rightarrow |\Upsilon(\mathbf{k})|^2$, which is what one sees in figure 1: the higher the energy of the ionized electron, the smaller the difference between the projection onto Coulomb waves and the projection onto plane waves.

Note that for atoms other than hydrogen, the energy eigenstates of the field-free Hamiltonian in equation (9) depend on radial wavefunctions, $R_{El}(r)$, and partial wave phase shifts, $\delta_l(k)$, that must be calculated numerically. The results for atomic hydrogen shown in figure 1 imply that the Fourier transform of the numerically calculated solution of the TDSE provides quite accurate results for the ionized electron probability distributions in energy (or momentum) provided the projection is carried out at a time, t_p , significantly later than the end of the laser pulse(s). This means that in this case, propagation of the numerical solution of the

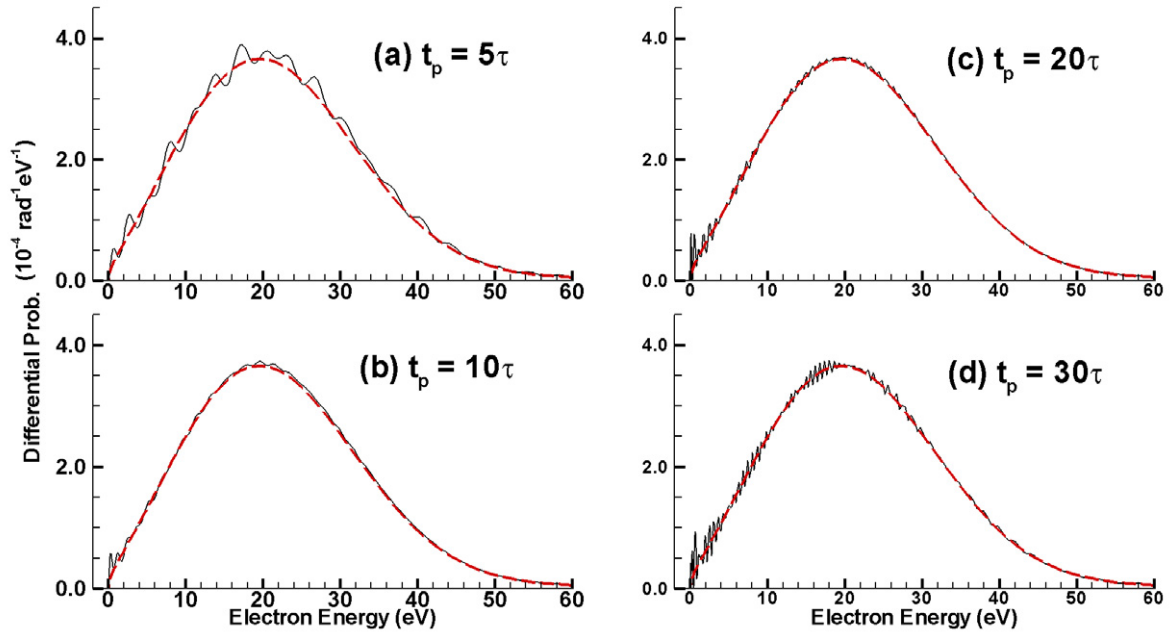


Figure 1. Energy distributions of electrons ionized from the H atom at the angle $\theta_k = \pi$ by a 2-cycle attosecond pulse of photon energy $\omega = 36$ eV and peak intensity $I_0 = 5 \times 10^{15}$ W cm $^{-2}$. The probability distributions calculated by projecting the numerical solution of the TDSE, $\Psi(\mathbf{r}, t_p)$, onto the (continuum) energy eigenstates of the field-free Hamiltonian (dashed curves) (cf equation (11)) are compared to the probability distributions calculated by projecting $\Psi(\mathbf{r}, t_p)$ onto plane waves (solid curves) (cf equation (17)) at different times, t_p , measured from the end of the attosecond pulse: (a) 5τ , (b) 10τ , (c) 20τ and (d) 30τ , where τ is the duration of the attosecond pulse, as defined in the text. Note that the dashed curve is, in principle, independent of t_p (and, in fact, is found numerically to be the same in each panel).

TDSE must be extended in time up to the chosen time, t_p , following the end of the laser pulse(s). Whether this represents more computational labor than calculating numerically the solutions of the field-free Hamiltonian is an issue to be considered in any particular calculation. Finally, the probability distributions predicted by projecting onto plane waves include unphysical rapid oscillations, particularly at low energies. Thus, any investigations that seek to obtain accurate predictions at low energies must project the solution of the TDSE onto the energy eigenstates of the field-free Hamiltonian. In the present paper, all energy or momentum distributions for the hydrogen atom are calculated by projecting the solution of the TDSE onto the Coulomb eigenstates of the field-free Hamiltonian. Only one of our results, for the He atom, is obtained by projecting the solution of the TDSE onto plane waves. However, this result for the He atom involves probabilities that are integrated over electron momenta. Thus, the rapid oscillations as a function of electron momentum that are introduced by the projection onto plane waves are expected to average out to a very good approximation. (For example, integration in energy of the two probability distributions for ionization of the H atom shown in each of the figures 1(c) and (d) give agreement within approximately 1%.)

3. Roles of frequency and intensity on attosecond CEP effects

In this section, we present numerical results that shed light on the roles of the frequency and intensity of a few-cycle attosecond XUV pulse with well-defined CEP in producing asymmetric ionized electron momentum distributions.

3.1. An approximate frequency–intensity scaling law

As the carrier frequency of a few-cycle XUV pulse changes, must the intensity of the pulse also change in order to observe similar CEP-induced asymmetries in the resulting ionized electron momentum distributions? One may expect to observe similar CEP-induced asymmetry effects produced by two few-cycle XUV pulses with different carrier wave frequencies provided the two pulses have similar peak values of their corresponding vector potentials. This expectation stems from the fact that electrons ionized at some point during a few-cycle pulse will receive an impulse by the remainder of the pulse. The magnitude of this impulse is equal to the value of the vector potential at the moment when the electron is ionized (see, e.g. [15, 21]). The magnitude of the XUV pulse’s vector potential depends on the pulse’s intensity and frequency as $A_0 \propto \sqrt{I_0}/\omega$ (cf equation (5) and the text that follows). Hence, it would seem that two few-cycle XUV pulses having equal CEPs but different frequencies, ω_1 and ω_2 , would produce similar ionized electron momentum distribution asymmetries provided that the peak intensities of the two XUV pulses, $I_0(1)$ and $I_0(2)$, are related as follows:

$$\sqrt{I_0(1)}/\omega_1 = \sqrt{I_0(2)}/\omega_2. \quad (20)$$

Two points should be mentioned in connection with this scaling law. Firstly, equation (20) is consistent with equality of the ponderomotive potentials associated with the two XUV pulses. Although, as noted by Lindner *et al* [22], ‘... the concept of the ponderomotive potential ... is questionable in the few-cycle regime,’ the concept of the vector potential becomes important in this regime. Interestingly, the two concepts have a simple (mathematical) relationship. Secondly, the similarity in the photoelectron energy distributions produced by XUV pulses of very different energies may not apply for atoms whose photoionization cross-sections have significant energy-dependent structure in the energy regions of interest. However, for atoms such as H and He, whose photoionization cross-sections decrease smoothly and monotonically with photon energy (as do the cross-sections for subshells of all atoms for energies far above their thresholds), the scaling law is expected to apply.

In order to test this scaling law, in figure 2, we compare the differential probability distributions of electrons ionized from the H atom at the angles $\theta_k = 0$ and π by two 2-cycle attosecond pulses having different photon energies, $\omega_1 = 36$ eV and $\omega_2 = 72$ eV, CEPs $\phi = 0.5\pi$, and various pairs of peak intensities, $I_0(1)$ and $I_0(2)$, which are indicated in the figure, with the intensity pairs in each row satisfying the scaling law in equation (20). Specifically, since the frequencies of the two XUV pulses differ by a factor of 2, the intensities must differ by a factor of 4. The asymmetries of the electron distributions are barely visible at the lowest pair of intensities. As the peak intensities $I_0(1)$ and $I_0(2)$ increase, respectively, to 5×10^{14} W cm⁻² in (b) and 2×10^{15} W cm⁻² in (e), one observes clearly the differences between the $\theta_k = 0$ and π energy distributions. At even higher pairs of peak intensities, as in (c) and (f), the differences become quite significant. As these numerical results indicate, the scaling law in equation (20) appears to be approximately satisfied, i.e. the asymmetries in the electron momentum distributions appear to have approximately similar shapes.

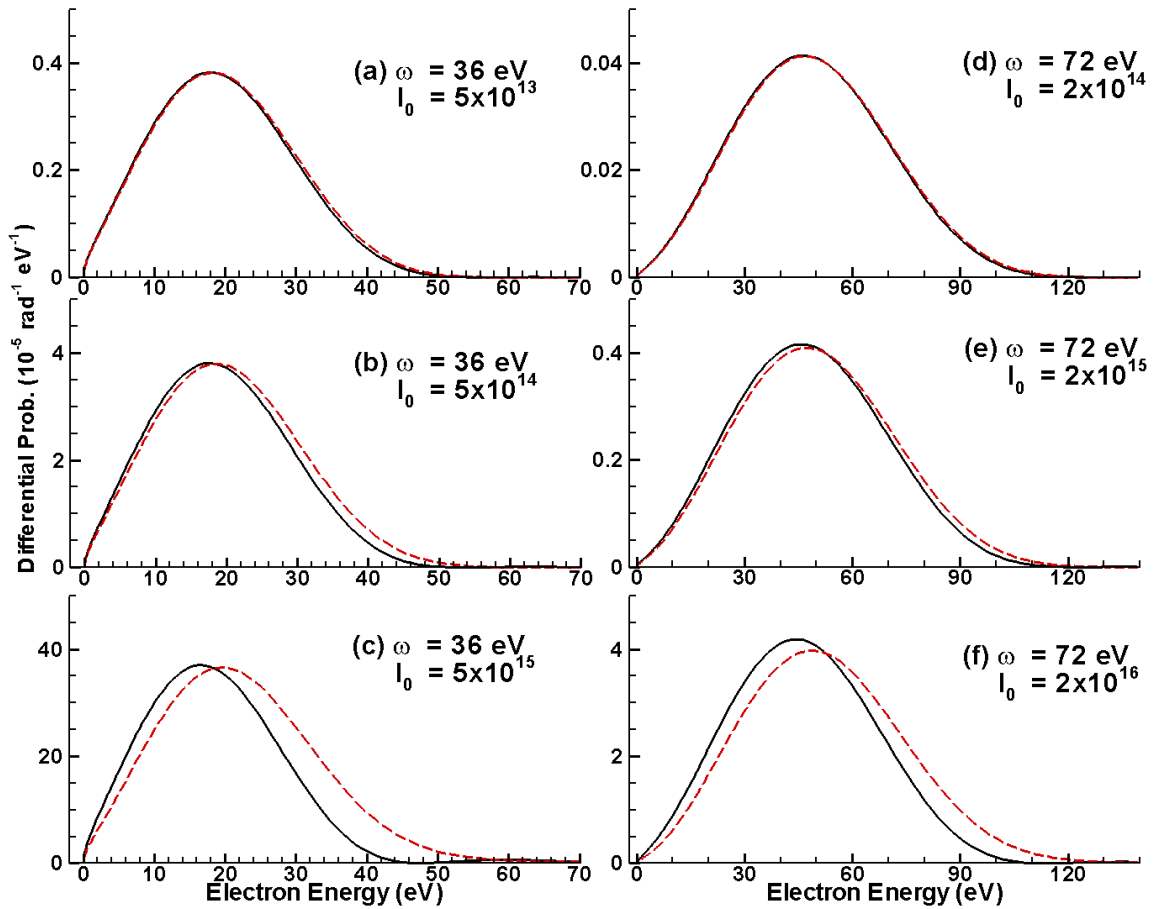


Figure 2. Comparison of the energy distributions of electrons ionized from the H atom at the angles $\theta_k = 0$ (solid curve) and $\theta_k = \pi$ (dashed curve) by a 2-cycle attosecond pulse having a CEP of 0.5π for two different photon energies: $\omega = 36$ eV ((a)–(c)) and 72 eV ((d)–(f)). For each photon energy, results are shown for three different attosecond pulse intensities (in W cm^{-2}), which are indicated in each plot. Note that the intensities for the two photon energies in each row (i.e. (a) and (d), (b) and (e), and (c) and (f)) correspond to the two attosecond pulses having the same peak value of the vector potential, i.e. they satisfy the approximate scaling law in equation (20).

Other features of the curves in figure 2 may be understood qualitatively. Consider first the energy spread of the electron momentum distribution. One observes that the higher the frequency, the larger is the energy spread of the electron momentum distribution. Using the uncertainty principle, for pulses having the same number of cycles, the energy uncertainty (calculated for an uncertainty in time equal to the pulse duration) is proportional to the frequency of each pulse. Thus, one expects the width in energy of the electron energy spectrum to be roughly proportional to the frequency of the few cycle pulse. One observes in figure 2 that indeed for frequencies differing by a factor of two, the spread in energy of the electron momentum distributions also differ roughly by a factor of two. Consider next the decrease in ionization probability with frequency. This is not so easily explained in a hand-waving way. However, one

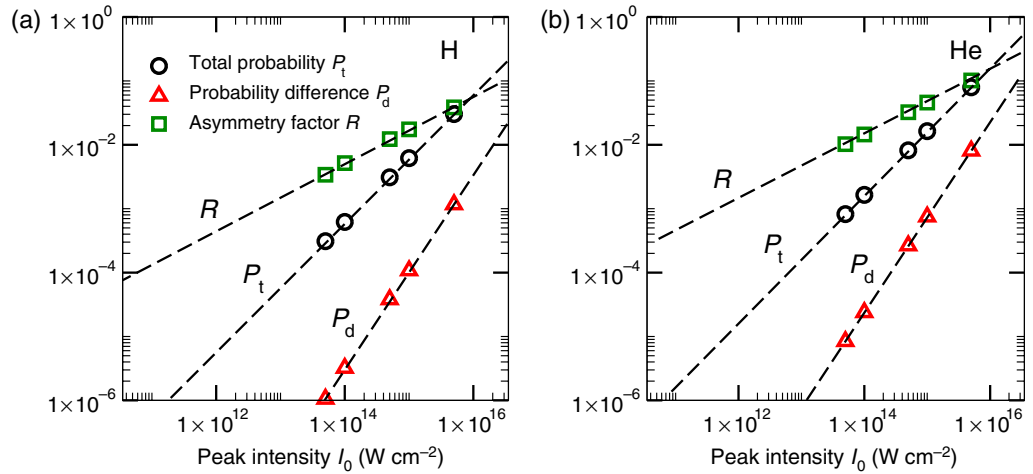


Figure 3. Comparison of the total ionization probability P_t (\circ), the probability difference P_d (Δ), and the asymmetry factor $R = P_d/P_t$ (\square) (cf equations (13) and (14)) as a function of the attosecond pulse peak intensity, I_0 , for (a) the H atom and (b) the He atom. The dashed lines are drawn through the data points to guide the eye. For H and He, the slopes of R , P_t and P_d for H (He) are 0.526 (0.498), 0.995 (0.993) and 1.521 (1.491), respectively; see text for discussion.

may show that the decrease is consistent with the decrease in the H atom photoionization cross-section as a function of frequency (taking into account also the spread in energy of the electron momentum distribution) given that the number of photons in each pair of pulses in figure 2 is approximately constant.

3.2. Intensity dependence of CEP-induced asymmetries

In order to investigate further the physical mechanisms of the CEP effects predicted in figure 2, it is useful to compare the total ionization probability, P_t , the probability difference, P_d , and the asymmetry factor R (cf equations (13) and (14) and the surrounding text), as a function of the peak intensity of the attosecond pulse. In figure 3, such comparisons are shown for both the H and the He atoms ionized by a 2-cycle attosecond pulse with photon frequency $\omega = 36$ eV and CEP $\phi = 0.5\pi$. One can deduce the slopes of P_t , P_d and R versus intensity from the log-log plots to be approximately 1.0, 1.5 and 0.5, respectively, for both H and He. These results imply that, although the total ionization probability P_t is mainly a one-photon process owing to its linear dependence on intensity, the probability difference P_d between the directions $k_z < 0$ and $k_z > 0$ is due to a nonlinear process owing to its dependence on the intensity raised to the power 1.5. A possible origin for the asymmetries induced by the attosecond CEP is therefore interference between one-photon and two-photon ionization processes.

Previous studies for other systems have indicated that asymmetries resulting from probes with few cycle pulses stem from nonlinear effects. In particular, control of the direction of emission of photoexcited electrons in semiconductors was demonstrated experimentally in [23]. In that work, the asymmetry of the electron emission was shown to result from quantum interference of electrons produced by one- and two-photon bound-free intersubband transitions in AlGaAs/GaAs quantum well superlattices. More recently, asymmetries in ionization of

Rydberg atoms by few-cycle radio-frequency pulses were attributed to interference between ionization amplitudes involving odd and even numbers of photons [24]. Most recently, Roudnev and Esry [25] have presented a general framework for understanding CEP effects in a quantum system interacting with an intense short laser pulse. Within their framework, all CEP asymmetry effects are interpreted as due to interference between transition amplitudes involving odd and even numbers of photons. Our numerical findings for the intensity dependences shown in figure 3 for ionization of the H and He atoms with few-cycle XUV pulses are consistent with results of these other references.

4. Role of an additional IR laser pulse

Recently, we have investigated CEP-induced asymmetries in the momentum and energy distributions of electrons ionized from both H and He atoms by either a single few-cycle attosecond pulse or two time-delayed attosecond pulses [13]. Additional insights into the CEP-induced asymmetries in the momentum and energy distributions of electrons ionized by a single few-cycle attosecond pulse have been provided in the prior section of this paper. Experimentally, isolated attosecond XUV pulses are typically synthesized from high-order harmonics generated by an intense IR laser pulse [1, 26]. Based on our demonstrated CEP-induced asymmetries in electron momentum and energy distributions produced by one or two few-cycle attosecond pulses, it is consequently of interest to examine what effect, if any, there will be on these attosecond pulse CEP-induced asymmetries in the presence of an additional IR pulse. We examine this question in this section, i.e. we investigate the momentum and energy distributions of electrons ionized by a single attosecond pulse in the presence of an additional IR pulse. We examine first the case of a weak, few-cycle IR pulse, which we find augments the attosecond pulse CEP-induced asymmetries. We then examine the case of a more intense, few-cycle IR pulse and find that it introduces additional asymmetries for low energy electrons, which we explore in some detail. In all our calculations, we assume the IR laser has a wavelength $\lambda_{\text{IR}} = 750 \text{ nm}$ and a duration of four cycles, $\tau_{\text{IR}} = 4T_{\text{IR}}$, unless otherwise stated. The value of the IR CEP phase, ϕ_{IR} , is set equal to either 0 or 0.5π in order that if the peak of the attosecond pulse occurs at the peak of the envelope of the IR pulse, then it will occur at either a zero or the peak of the IR carrier wave's vector potential.

It is important to note that it is not necessary to have either a few-cycle or an intense attosecond pulse to produce asymmetric photoelectron distributions in the presence of an IR pulse (see, e.g. [10]–[12]). The (additional) asymmetry induced by an IR pulse is directly related to the value of the IR field's vector potential at the time of ionization by the XUV pulse. Our focus here, however, remains on exploring the sensitivity of the asymmetric photoelectron momentum and energy distributions, produced in the presence of both IR and few-cycle XUV pulses, on the CEP of the XUV pulse.

4.1. Augmentation of attosecond pulse CEP effects by a weak, few-cycle IR pulse

In figure 4, we show the energy distributions of electrons ionized from the H atom in opposite directions along the laser polarization axis (i.e. at the angles $\theta_k = 0$ and $\theta_k = \pi$) by a 2-cycle attosecond pulse with photon energy $\omega = 36 \text{ eV}$ and peak intensity $I_0 = 5 \times 10^{15} \text{ W cm}^{-2}$ in the presence of an additional IR pulse of intensity $I_{\text{IR}} = 5 \times 10^{11} \text{ W cm}^{-2}$. In the left-hand column of figure 4, the attosecond pulse is put at the zero of the IR vector potential (cf figure 4(e)).

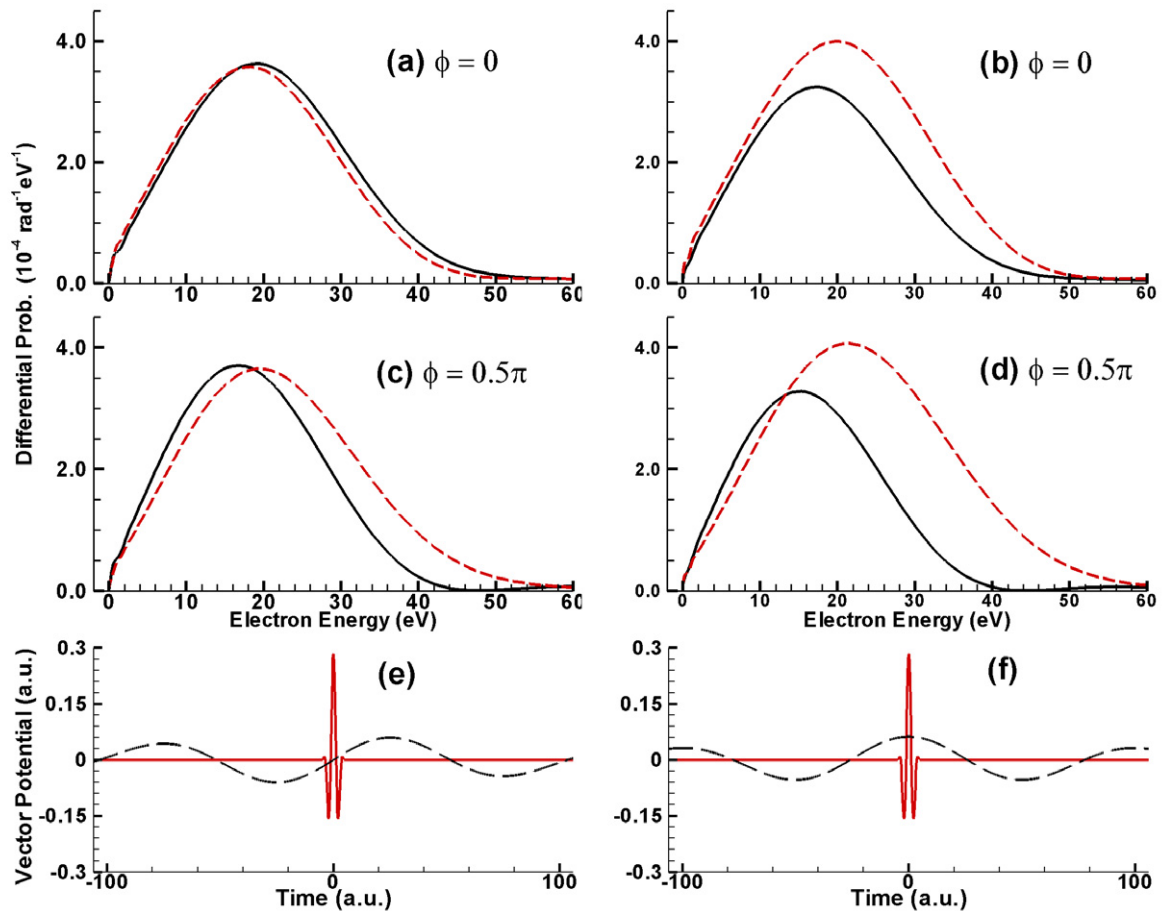


Figure 4. Energy distributions of electrons ionized from the H atom at the angles $\theta_k = 0$ (solid curve) and $\theta_k = \pi$ (dashed curve) by a 2-cycle attosecond pulse, having photon energy $\omega = 36 \text{ eV}$ and peak intensity $I_0 = 5 \times 10^{15} \text{ W cm}^{-2}$, in the presence of an additional 4-cycle IR laser pulse with wavelength $\lambda_{\text{IR}} = 750 \text{ nm}$ and peak intensity $I_{\text{IR}} = 5 \times 10^{11} \text{ W cm}^{-2}$. The CEP of the attosecond pulse is indicated in each plot. The attosecond pulse is positioned at the zero of the IR vector potential in the first column and at its peak in the second column. In panels (e) and (f), we show the vector potentials of the attosecond pulse (solid curve) and (the central part of) the IR pulse (long dash curve) corresponding to the results shown in (c) and (d), respectively.

In this case, the electron energy distributions are almost identical with those obtained in the absence of an IR laser pulse (e.g. compare figures 2(c) and 4(c)). However, when the attosecond pulse is put at the peak of the vector potential (cf figure 4(f)), as in the results shown in the right-hand column of figure 4, the asymmetries between the two emission angles are greatly increased, both for an attosecond CEP of $\phi = 0$ (figure 4(b)) and one of 0.5π (figure 4(d)). However, the asymmetry is clearly larger when $\phi = 0.5\pi$, as is the case when there is no IR laser field.

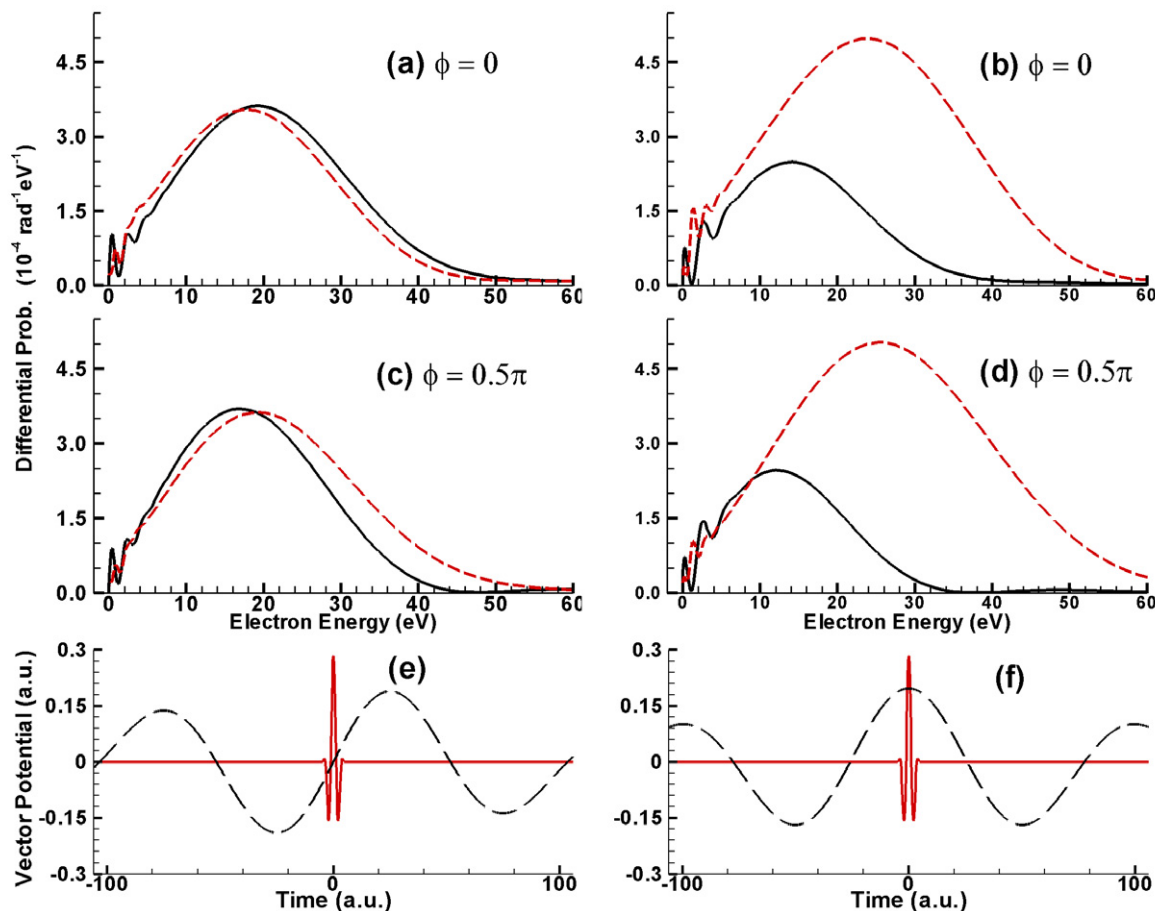


Figure 5. The same as figure 4 except that the IR pulse has a peak intensity of $I_{\text{IR}} = 5 \times 10^{12} \text{ W cm}^{-2}$.

In figure 5, we show similar ionized electron energy distributions for the case of a somewhat greater IR pulse peak intensity, $I_{\text{IR}} = 5 \times 10^{12} \text{ W cm}^{-2}$. In the case that the attosecond pulse is put at the zero of the IR vector potential (shown in the left-hand panels of figure 5), we again observe that the electron distributions and their asymmetries are similar to the case in which there is no IR field (e.g. compare figures 2(c) and 5(c)), at least for electron kinetic energies above approximately 6 eV. In contrast to this largely null effect of the IR pulse, in the case that the attosecond pulse is put at the peak of the IR vector potential (shown in the right-hand panels of figure 5), the asymmetries between the two emission angles are significantly augmented compared with those in figures 4(b) and (d). Comparing figures 5(b) and (d), we see that the ionized electron momentum distributions are still sensitive to the CEP of the XUV pulse; however, the augmented asymmetries in the presence of the IR pulse are so large that one must look carefully to see the sensitivity of the distributions to the XUV CEP. The low-energy structures in the electron energy distributions that appear in figure 5 but not in figure 4 are examined in detail in the next section.

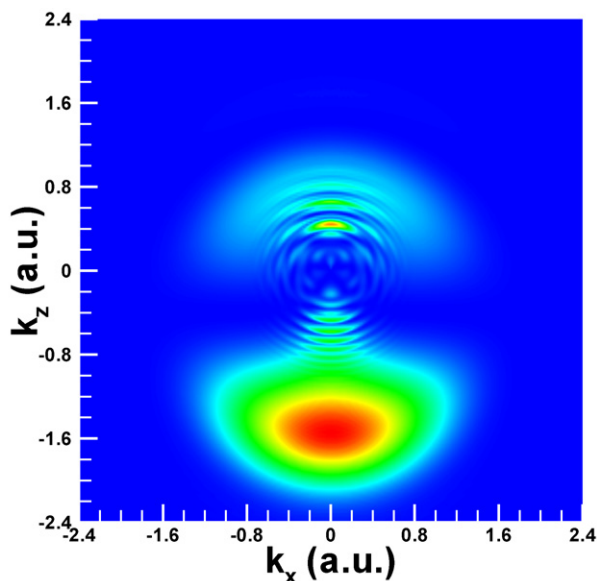


Figure 6. Momentum distribution of electrons ionized from the H atom by a 2-cycle attosecond pulse with photon energy $\omega = 36$ eV and peak intensity $I_0 = 5 \times 10^{15} \text{ W cm}^{-2}$ in the presence of an 8-cycle IR pulse with wavelength $\lambda_{\text{IR}} = 750$ nm and peak intensity $I_{\text{IR}} = 2 \times 10^{13} \text{ W cm}^{-2}$. The CEP of the attosecond pulse is 0.5π . The attosecond pulse is positioned at the peak of the IR vector potential, as shown (for a different IR pulse peak intensity) in figure 5(f).

4.2. Low-energy structures appearing in the presence of an intense IR pulse

As shown in figure 5, the energy distributions of electrons ionized from the H atom by a few-cycle XUV pulse in the presence of a moderately intense few-cycle IR pulse develop clearly visible structures for electron kinetic energies less than approximately 6 eV. These structures are not present in the absence of the IR pulse (cf figure 2); neither are they present in the case of a weak IR pulse (cf figure 4). In order to investigate these new features, we further increase the IR laser peak intensity to $2 \times 10^{13} \text{ W cm}^{-2}$ and also double the IR pulse duration to 8 cycles. The resulting ionized electron momentum distributions in the k_x - k_z -plane are shown in figure 6. The momentum distributions clearly exhibit ring or arc structures for both $k_z > 0$ and $k_z < 0$. It is also clear that these ring or arc structures have different spacings for $k_z > 0$ and $k_z < 0$. Consequently, they may result from different physical mechanisms, as discussed below.

The results in figure 6 show clearly that the electrons escape predominantly in the $k_z < 0$ direction. The entire asymmetric spectrum is shifted down by the IR vector potential towards negative values of k_z . The ring or arc structures observed in figure 6 are reminiscent of the interference patterns that have been observed or predicted between electron wave packets produced by two or more attosecond pulses [13]–[15] or even between electron wave packets produced by each half cycle of a few-cycle femtosecond laser pulse [21]. Neither of those situations, however, apply in the present case. Firstly, we only have one few-cycle attosecond pulse and not two. Secondly, even though we have a few-cycle (XUV) pulse, as shown in figure 2, there are no interference patterns in the electron momentum distributions in the absence

of the IR pulse (as might be expected, owing to the large energies of the electron wave packets produced by XUV pulses as compared to those produced by few-cycle femtosecond pulses).

The ring or arc structures observed in figure 6 originate from production of ionized electrons by a few-cycle attosecond XUV pulse in the presence of an IR pulse. Moreover, the IR pulse must have some minimum intensity for the rings or arcs to occur, as comparison of figures 4 and 5 shows. One must keep in mind also that the rings or arcs occur in a region of low electron energies, so that the Coulomb field of the nucleus should exert a significant influence. In fact, we have done exploratory strong field approximation (SFA) calculations (which ignore the Coulomb potential) and find that the ring or arc structures are absent in the SFA results for ionized electron momenta. Hence, it seems that the Coulomb field plays an important role or even more than one role. The possible roles of the Coulomb field include rescattering of the low-energy electrons driven by the IR field and/or allowing absorption of IR field photons when electrons pass near the nuclear potential. (According to our estimates, the IR field is too weak to ionize electrons significantly from the ground state of the H atom.)

Regarding IR field-driven rescattering of low-energy electrons, we observe that there is an asymmetry in such rescattering in this problem. As shown in figure 6, the IR field shifts the $k_z > 0$ part of the ionized electron spectrum closer to $k_z = 0$ and shifts the lowest energy part to negative values, $k_z < 0$. A corresponding shift occurs in coordinate space, i.e. the ionized electrons are shifted toward negative z . Thus, there may be significant rescattering by the Coulomb potential of some of the low-energy electrons (i.e. the ones ionized initially with $k_z > 0$, but shifted by the IR field to $k_z < 0$), assisted by the IR laser electric field. If so, the electrons that are thus rescattered (and that thus take positive values of momentum once again) may interfere with $k_z > 0$ electrons that are shifted by the IR pulse to lower positive momenta but which do not rescatter from the Coulomb potential. Having two groups of electrons with the same positive momenta that arrive at these momenta in different ways leads to interference of their respective transition amplitudes. This may be the mechanism for the structures appearing in the $k_z > 0$ part of the momentum spectrum.

On the other hand, those ionized electrons that are initially ionized with negative momenta, $k_z < 0$, will be shifted by the IR pulse to even greater negative momenta. Since ionization occurs at the peak of the IR pulse envelope, when the IR pulse electric field eventually changes sign, its magnitude will be insufficient to rescatter the electrons (initially produced with negative momenta) from the nuclear Coulomb potential. In this case, the Coulomb field can only facilitate absorption of IR field photons by low energy electrons located initially near the nucleus.

The foregoing observations and speculations on the origins of the low energy ring or arc structures in figure 6 seem plausible. However, a more careful examination of the low energy structures and their dependence on the various parameters in the problem is necessary. In what follows, we present some additional results that provide further information on the problem.

In order to see the low-energy structures clearly, we plot in figure 7 the ionized electron energy distributions at the angles $\theta_k = 0$ and $\theta_k = \pi$ corresponding to the ionized electron momentum distribution shown in figure 6. Examination of this figure shows that the prominent ring or arc structures are spaced in energy by $2\omega_{\text{IR}}$ for $\theta_k = 0$ (cf figure 7(a)) and by ω_{IR} for $\theta_k = \pi$ (cf figure 7(b)). For electron kinetic energies smaller than approximately 3.0 eV, there exist small, more closely spaced peaks in both cases. For $k_z < 0$ (cf figure 7(b)), the peaks for energies above about 3.0 eV are structureless, while for $k_z > 0$ (cf figure 7(a)) the three peaks above about 3.0 eV each have sidebands on each side of the main peak. For $k_z > 0$, the spacing of the main peaks by $2\omega_{\text{IR}}$ is reminiscent of observations of such spacing when the

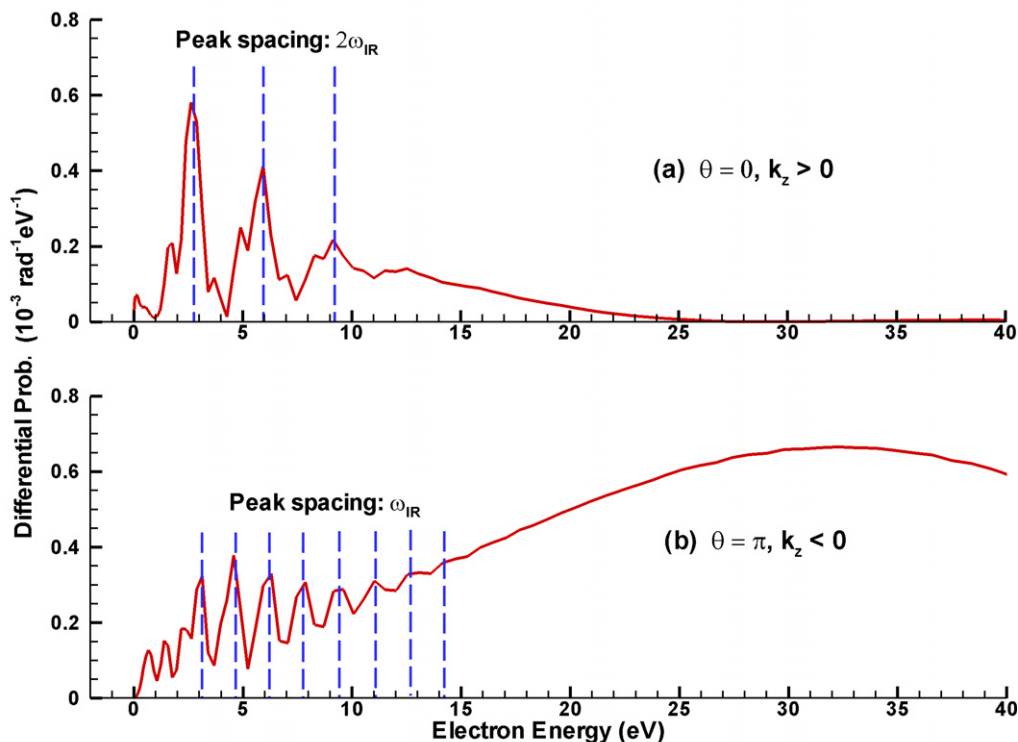


Figure 7. Energy distributions of electrons ionized from the H atom (by an attosecond XUV pulse in the presence of an IR pulse) in opposite directions along the laser field polarization axis: (a) $\theta_k = 0$ and (b) $\theta_k = \pi$. All laser parameters are the same as in figure 6. For greater clarity, only the parts of the energy spectra below 40 eV are shown. Dashed lines (meant to guide the eye) are spaced by $2\omega_{\text{IR}}$ in (a) and by ω_{IR} in (b); see text for discussion.

ionized electrons are produced by two attosecond pulses spaced by half an IR field period [15]. Here, of course, we have only a single attosecond pulse. However, could rescattering of low-energy ionized electrons by the Coulomb field, driven every half cycle by the IR field, lead to the interference suggested above that would produce such spacing by $2\omega_{\text{IR}}$? Interestingly, exactly halfway between the peaks that are spaced by $2\omega_{\text{IR}}$, the $k_z > 0$ spectrum shows minima. This possible destructive interference of a peak halfway between others separated by $2\omega_{\text{IR}}$ is reminiscent of interference effects studied by Vénard *et al* [27] in photoelectron spectra produced by neighboring odd harmonics in the presence of the IR field that produced the harmonics. It was found that the strength of the even harmonic between the two neighboring odd harmonics was very sensitive to the relative phases of the three light fields (i.e. both constructive and destructive interference were demonstrated). Of course, in our case we have a very broad XUV pulse in the presence of an IR field and not a harmonic spectrum of the IR field; also, the structures we observe occur only for low electron energies and differ significantly for positive and negative electron momenta along the z -axis. For these reasons, we expect that any interference is more likely to be due to laser-assisted electron scattering effects (and, in particular, to laser-induced electron rescattering effects, which occur in only one direction) than to three-color interference effects such as those investigated in [27].

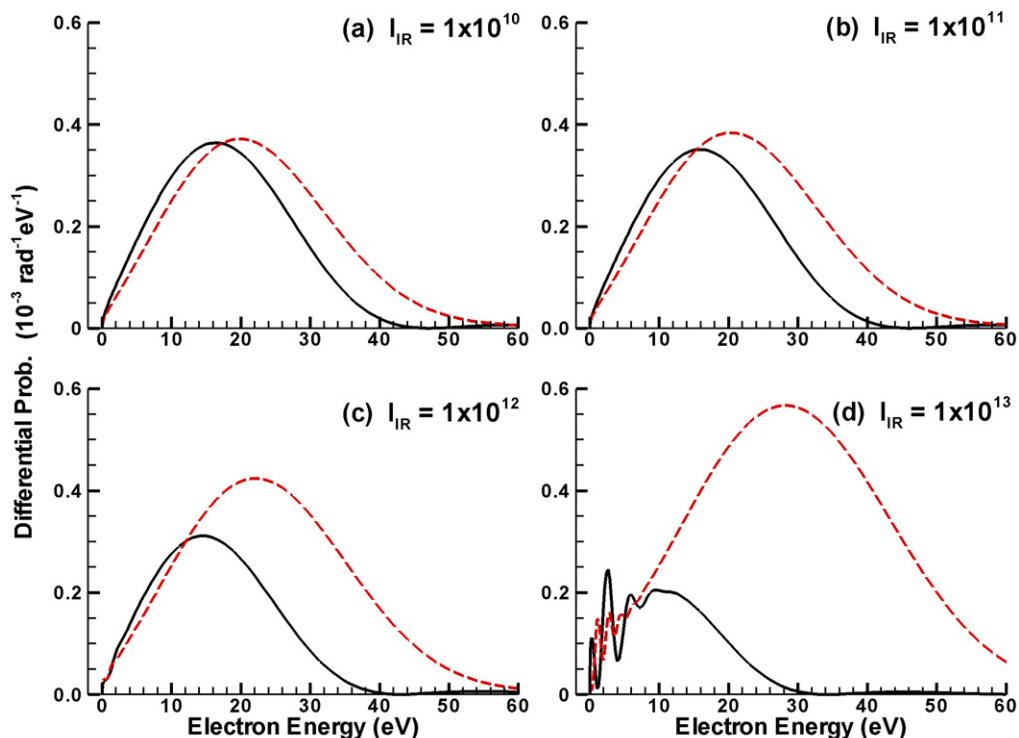


Figure 8. Energy distributions of electrons ionized from the H atom at the angles $\theta_k = 0$ (solid curve) and $\theta_k = \pi$ (dashed curve) by a 2-cycle attosecond pulse with photon energy $\omega = 36$ eV and peak intensity $I_0 = 5 \times 10^{15}$ W cm $^{-2}$ in the presence of an additional 4-cycle IR laser pulse with wavelength $\lambda_{\text{IR}} = 750$ nm at four different peak intensities I_{IR} (W cm $^{-2}$), shown in each plot. The CEP of the attosecond pulse is 0.5π . The attosecond pulse is positioned at the peak of the IR vector potential, as shown (for different field parameters) in figure 5(f).

In figure 8, we show how the low energy structures evolve with increasing IR pulse intensity. One sees the beginning of some structure close to zero momentum in figure 8(c) corresponding to an IR peak intensity of $I_{\text{IR}} = 1 \times 10^{12}$ W cm $^{-2}$. When the IR peak intensity is increased to 1×10^{13} W cm $^{-2}$, one sees in figure 8(d) that the low energy structures are well developed. The results in this figure also show how the attosecond pulse CEP-induced asymmetries in the ionized electron momentum and energy distributions are progressively augmented by the IR field as its peak intensity increases.

In figure 9, we show how the ionized electron momentum and energy spectra vary with increasing XUV pulse intensity for the case of a fixed, intense IR pulse. One sees that the magnitudes of the probabilities for ionization scale linearly with the XUV pulse intensity, as expected for a predominantly one-photon process. In particular, the low-energy structures scale in magnitude with the XUV pulse intensity as well. For this case of a relatively intense IR pulse (but not so intense that ionization before the XUV pulse is significant), one sees that the asymmetries in the spectra for positive and negative electron momenta are largely due to the interaction with the IR pulse, in particular, because in this figure the XUV CEP is zero.

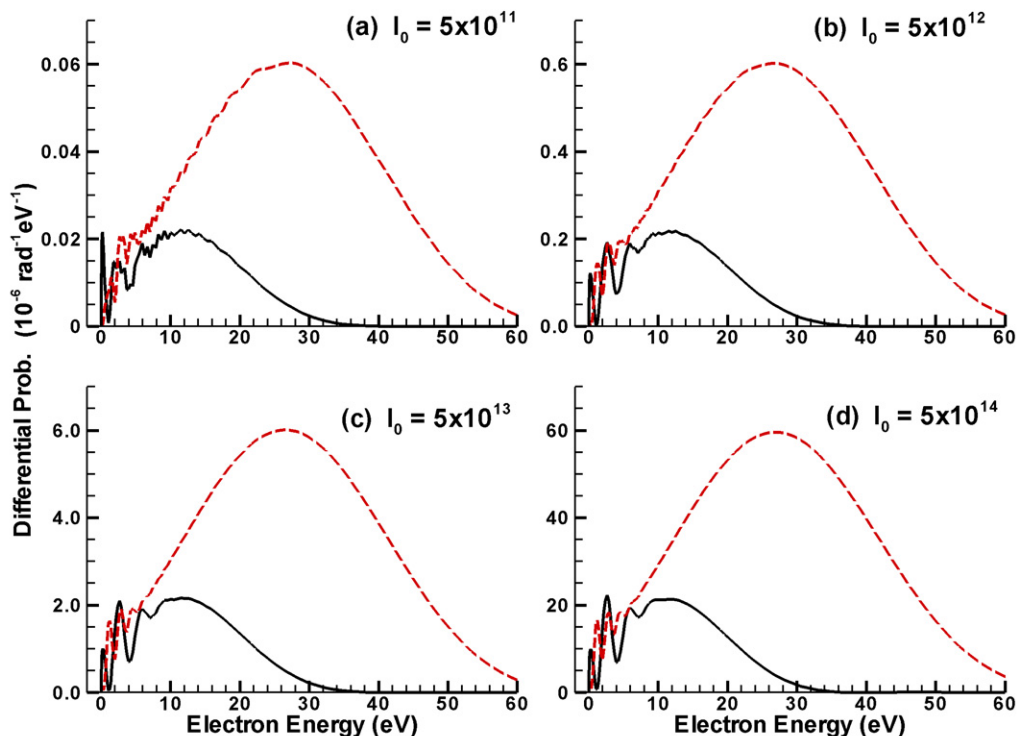


Figure 9. Energy distributions of electrons ionized from the H atom at the angles $\theta = 0$ (solid curve) and $\theta = \pi$ (dashed curve) by a 2-cycle attosecond pulse with photon energy $\omega = 36$ eV and four different peak intensities I_0 (W cm^{-2}) (indicated in each plot) in the presence of an additional 4-cycle IR laser pulse with wavelength $\lambda_{\text{IR}} = 750$ nm and peak intensity $I_{\text{IR}} = 1 \times 10^{13}$ W cm^{-2} . The CEP of the attosecond pulse is 0. The attosecond pulse is positioned at the peak of the IR vector potential.

Finally, in figure 10, we show how the ionized electron momentum and energy spectra vary with the energy of the XUV pulse for two different XUV pulse lengths. As may be expected, the difference in ionized electron probabilities for positive and negative momenta is greater for lower XUV energies, since the relative effect of the IR pulse on the ionized electrons is greater the slower the electrons. Remarkably, the results for 4-cycle XUV pulses show no evidence of any low energy structure. This is so because the XUV pulse energy is large enough that its width in energy for the case of a 4-cycle pulse does not result in production of electrons with energies near zero energy. Hence, rescattering of slow electrons by the IR pulse in this case is apparently not possible (or at least not significant), unlike the case of a 2-cycle XUV pulse. The 4-cycle results also show that ATI of ground state electrons by the IR pulse during ionization by the attosecond XUV pulse is not significant, since no IR ATI structure is visible.

To summarize our interpretation of the low-energy structures observed in figures 6–10, it seems likely that they originate from the different dynamics experienced by negative and positive momentum electrons as a result of their interaction with the attractive Coulomb field and the few-cycle IR laser pulse both during and subsequent to their ionization by the attosecond XUV pulse. For the polarization direction of the IR electric field that we have chosen at the time

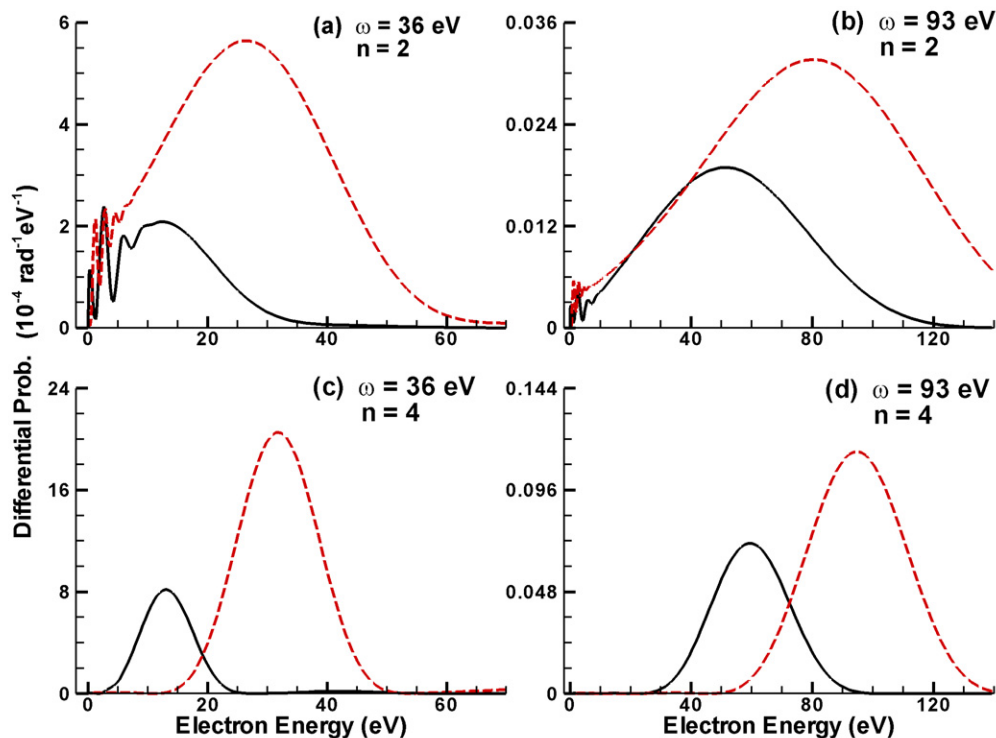


Figure 10. Comparison of energy distributions of electrons ionized from the H atom at the angles $\theta_k = 0$ (solid curves) and $\theta_k = \pi$ (dashed curves) by a single attosecond pulse with two different photon energies, $\omega = 36$ eV ((a) and (c)) and 93 eV ((b) and (d)), in the presence of an additional 4-cycle IR laser pulse with wavelength $\lambda_{\text{IR}} = 750$ nm and peak intensity $I_{\text{IR}} = 1 \times 10^{13}$ W cm $^{-2}$. The attosecond pulse, with CEP $\phi = 0$ and peak intensity $I_0 = 5 \times 10^{15}$ W cm $^{-2}$, is positioned at the peak of the IR vector potential. The number of cycles of the attosecond pulse is $n = 2$ in the upper row and $n = 4$ in the lower row.

of ionization by the XUV pulse, newly ionized electrons having initially negative momenta will be accelerated by the IR field for half an IR period towards larger negative momenta. In contrast, newly ionized electrons having positive momentum will be decelerated for half an IR period toward smaller positive momenta or even toward negative momenta (if their initial positive momentum is small). Since the attosecond XUV pulse gives most electrons a substantial energy and momentum, it is to be expected that most electrons having initially negative momenta (which are shifted initially by the IR potential to even larger negative momenta) will not be rescattered by the nuclear Coulomb potential when the electric field of the IR pulse changes sign. Moreover, absorption of IR photons by low-energy electrons as they leave the vicinity of the nucleus may produce the peaks spaced by ω_{IR} that are observed in the momentum spectrum for $k_z < 0$.

The situation appears to be quite different for the $k_z > 0$ electron energy spectrum. Although all electrons having an initially positive momentum will be shifted by the IR pulse to smaller momentum values (i.e. they experience a negative impulse), most will still have positive momenta at the time the IR electric field changes sign. The electrons having initially

the smallest positive momenta may, however, be shifted to negative momenta by the negative impulse of the IR electric field. In this case, they may be elastically scattered by the nuclear Coulomb potential to positive momenta. Thus, the rescattered electrons having small positive momenta may interfere with electrons that were ‘downshifted’ by the IR pulse from larger positive momenta to the same small values of positive momenta. The transition amplitudes for these two different groups of electrons will thus interfere. Since this process is expected to happen within a half-cycle of the IR pulse, this hypothetical scenario may be consistent with the $2\omega_{\text{IR}}$ spacing predicted numerically in figure 7(a). Of course, slow electrons in this scenario may also be expected to absorb IR photons as they rescatter from the nuclear Coulomb potential. Why there exist minima between the prominent peaks that are spaced by $2\omega_{\text{IR}}$ is unclear to us; nor are we able to explain the origin of the sidebands on either side of the prominent peaks. Clearly, understanding the role of rescattering of low energy electrons in producing these low-energy structures in the momentum distributions warrants further investigations.

5. Summary and conclusions

In summary, in this paper, we have investigated the role of the CEP of a few-cycle attosecond pulse on ionized electron momentum and energy distributions. We have proposed an approximate scaling law relating the frequency and intensity of the few-cycle attosecond pulse that allows one to expect similarly-shaped asymmetries in ionized electron momentum and energy spectra as either the frequency or the intensity of the attosecond pulse is varied. We have also determined the intensity dependence of these asymmetries. Finally, we have presented a detailed examination of the role of an additional few-cycle IR pulse.

We conclude that our numerical results are consistent with the interpretation that CEP-induced asymmetries originate from interference between one- and two-photon ionization transition amplitudes for the attosecond pulse even though the total ionization rate is consistent with a single-photon process. Our scaling law for the frequency and intensity of the attosecond pulse (for a fixed number of cycles per pulse) allows one to estimate approximately how the CEP-induced asymmetries in ionized electron momentum and energy spectra will change with varying attosecond pulse parameters. Finally, we have shown how even a weak additional IR pulse can significantly augment the CEP-induced asymmetries of an attosecond pulse. In addition, for short attosecond pulses producing an electron energy spectrum having significant numbers of low-energy electrons, we have shown that the IR field may allow one to explore rescattering of the ionized electron from the ionic core of the ionized atom.

Acknowledgments

We gratefully acknowledge stimulating and useful conversations and correspondence with Mikhail V Frolov, Chii-Dong Lin, Nikolai L Manakov and Toru Morishita. This work was completed utilizing the Research Computing Facility associated with the USCMS Tier-2 site at the University of Nebraska—Lincoln. It was supported in part by the Department of Energy, Office of Science, Division of Chemical Sciences, Geosciences and Biosciences under grant no. DE-FG02-96ER14646. LYP acknowledges also partial support of the National Natural Science Foundation of China under grant no. 10704003.

References

- [1] Sansone G *et al* 2006 *Science* **314** 443
- [2] Cormier E and Lambropoulos P 1998 *Eur. Phys. J. D* **2** 15
- [3] de Bohan A, Antoine P, Milošević D B and Piraux B 1998 *Phys. Rev. Lett.* **81** 1837
- [4] Christov I P 1999 *Opt. Lett.* **24** 1425
- [5] Paulus G G, Grasbon F, Walther H, Villorrese P, Nisoli M, Stagira S, Priori E and De Silvestri S 2001 *Nature* **414** 182
- [6] Paulus G G, Lindner F, Walther H, Baltuška A, Goulielmakis E, Lezius M and Krausz F 2003 *Phys. Rev. Lett.* **91** 253004
- [7] Brabec T and Krausz F 2000 *Rev. Mod. Phys.* **72** 545
- [8] Milošević D B, Paulus G G, Bauer D and Becker W 2006 *J. Phys. B: At. Mol. Opt. Phys.* **39** R203
- [9] Verhoef A J, Fernández A, Lezius M, O'Keefe K, Uiberacker M and Krausz F 2006 *Opt. Lett.* **31** 3520
- [10] Bandrauk A D, Chelkowski S and Shon N H 2002 *Phys. Rev. Lett.* **89** 283903
- [11] Goulielmakis E *et al* 2004 *Science* **305** 1267
- [12] Bandrauk A D, Chelkowski S and Shon N H 2003 *Phys. Rev. A* **68** 041802
- [13] Peng L-Y and Starace A F 2007 *Phys. Rev. A* **76** 043401
- [14] Remetter T *et al* 2006 *Nat. Phys.* **2** 323
- [15] Varjú K *et al* 2006 *J. Phys. B: At. Mol. Opt. Phys.* **39** 3983
- [16] Peng L-Y and Starace A F 2006 *J. Chem. Phys.* **125** 154311
- [17] Hartree D R 1957 *The Calculation of Atomic Structures* (New York: Wiley) section 2.5
- [18] Chelkowski S, Bandrauk A D and Apolonski A 2004 *Phys. Rev. A* **70** 013815
- [19] Roy A K, Gupta N and Deb B M 2001 *Phys. Rev. A* **65** 012109
- [20] Yudin G L, Chelkowski S, Itani J, Bandrauk A D and Corkum P B 2005 *Phys. Rev. A* **72** 051401
- [21] Hu S X and Starace A F 2003 *Phys. Rev. A* **68** 043407
- [22] Lindner F, Schätzel M G, Walter H, Baltuška A, Goulielmakis E, Krausz F, Milošević D B, Bauer D, Becker W and Paulus G G 2005 *Phys. Rev. Lett.* **95** 040401
- [23] Dupont E, Corkum P B, Liu H C, Buchanan M and Wasilewski Z R 1995 *Phys. Rev. Lett.* **74** 3596
- [24] Gürtler A, Robicheaux F, van der Zande W J and Noordam L D 2004 *Phys. Rev. Lett.* **92** 033002
- [25] Roudnev V and Esry B D 2007 *Phys. Rev. Lett.* **99** 220406
- [26] Kienberger R *et al* 2004 *Nature* **427** 817
- [27] Véliard V, Taïeb R and Maquet A 1996 *Phys. Rev. A* **54** 721